optica

Second-harmonic generation of spatiotemporal optical vortices and conservation of orbital angular momentum

S. W. Hancock, S. Zahedpour, and H. M. Milchberg*

Institute for Research in Electronics and Applied Physics, University of Maryland, College Park, Maryland 20742, USA
**Corresponding author: milch@umd.edu*

Received 12 February 2021; revised 24 March 2021; accepted 25 March 2021 (Doc. ID 422743); published 27 April 2021

A spatiotemporal optical vortex (STOV) is an intrinsic optical orbital angular momentum (OAM) structure in which the OAM vector is orthogonal to the propagation direction [Optica 6, 1547 (2019)] and the optical phase circulates in space-time. Here, we experimentally and theoretically demonstrate the generation of the second harmonic of a STOV-carrying pulse along with the conservation of STOV-based OAM. Our experiments verify that photons can have intrinsic orbital angular momentum perpendicular to their propagation direction.

https://doi.org/10.1364/OPTICA.422743

A spatiotemporal optical vortex (STOV) [1,2] is an electromagnetic structure with orbital angular momentum (OAM) and optical phase circulation defined in spacetime and is supported by a polychromatic pulse [3]. For a STOV-carrying pulse propagating in free space [2], the OAM vector is perpendicular to the direction of propagation. This contrasts with a conventional space-defined optical vortex, which can be supported by a monochromatic beam, and where the OAM vector is parallel/anti-parallel to the direction of propagation and the optical phase winding is in the plane transverse to propagation. Examples of the latter include Bessel–Gauss (BG_l) or Laguerre–Gaussian (LG_{pl}) modes with nonzero azimuthal index l [4–7]. STOVs were first measured [1] as naturally emergent from filamentation processes in material media and can be constructed using a $4f$ pulse shaper as originally proposed in [8], with free-space STOV propagation from near field to far field first demonstrated in [2,9] and later confirmed in the far field by [10].

In second-harmonic generation (SHG) ($\omega \rightarrow 2\omega$) of conventional Laguerre Gaussian OAM beams, the second-harmonic photons carry twice the OAM of fundamental beam photons ($l\hbar \rightarrow 2l\hbar$) [11–15], where l is the OAM quantum number, here the beam topological charge. Similarly, in sum or difference frequency generation, the OAM of two fundamental modes are added [16]. In the case of q^{th}-order high harmonic generation with a mode of charge l, the resulting photons have OAM $ql\hbar$ [17–20]. The conservation of conventional OAM under these wide conditions has prompted measurements of harmonic generation and OAM conservation with STOV-carrying pulses as first presented in [21,22].

In this Letter, we demonstrate, for the first time to our knowledge, the SHG of STOVs and conservation of STOV OAM. Because SHG is fundamentally an interaction process of the quantized electromagnetic field, and because all photons in the STOV pulse from our pulse shaper carry the same bandwidth, polarization, and spatiotemporal (or spatiospectral) phase, our results verify that individual photons can have OAM orthogonal to their direction of propagation. To perform the measurements, we use a single-shot measurement technique [2,23] that captures the fundamental and SHG STOV amplitude and phase structure in mid-flight. Accompanying the measurements are simulations exploring the conversion process and the propagation of STOVs in material media.

Fundamental ($\lambda_0 = 800$ nm) STOVs with electric field E_S were generated by 50 fs pulses from a 1 kHz Ti:sapphire amplifier routed through the $4f$ pulse shaper depicted in Fig. 1(a) as first presented in Refs. [2,8,9]. The key feature of the pulse shaper is the transmissive fused silica phase plate at the common focus of the cylindrical lenses (the Fourier plane of the pulse shaper). The phase plate has a π step of height $\lambda_0/2(n_{FS} - 1) \sim 882$ nm (where $n_{FS} = 1.4533$ is the refractive index of the substrate at 800 nm) across its diameter. Orienting the step at $\alpha = \pm 40°$ to the dispersion direction of the input diffraction gratings generates fundamental STOVs E_S with topological charge $l = \pm 1$ in the near field of the pulse shaper. Alternatively, a spiral phase plate could have been used to generate a similar STOV in the far field of the shaper [2,9]. The angle α depends on the beam diameter and spectral resolution of the pulse shaper and is tuned experimentally. SHG of E_S was accomplished by placing a 100 μm thick, type I beta-barium borate (BBO) crystal at the immediate output of the $4f$ pulse shaper in the near field. The crystal was sufficiently thin to ensure SHG phase matching over the full pulse bandwidth. *It is important to stress here that a well-aligned, ideal pulse shaper of this type* [2,8,9] *imposes the same bandwidth, spatiotemporal phase, and polarization on all output photons*. In addition, the photons have a purely *spatial* phase, which is related to their extrinsic OAM. Minus this component, STOV-based OAM is intrinsic, and it is the intrinsic part of the OAM that is responsible for angular momentum conservation under SHG.

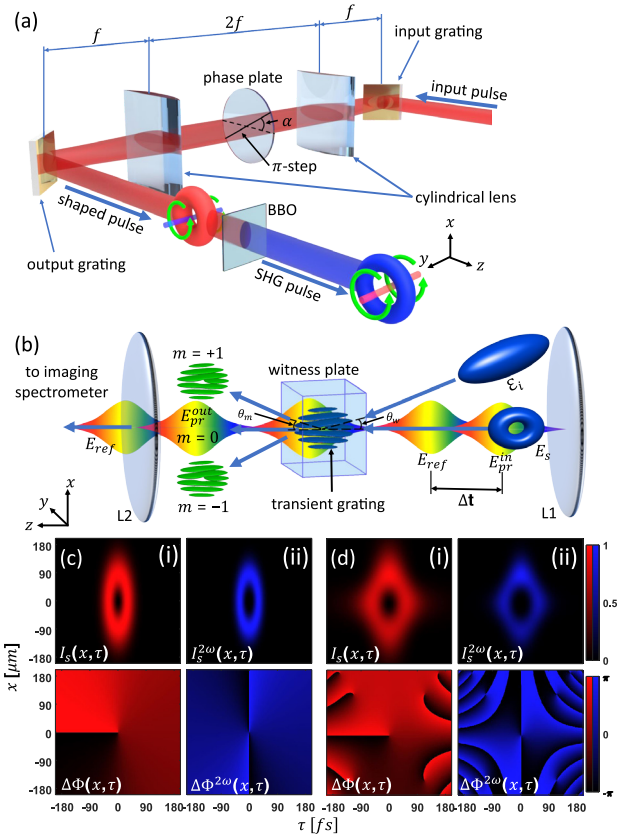

Fig. 1. (a) 4 f pulse shaper used to generate a $l = \pm 1$ STOV-carrying pulse at 800 nm, composed of two 1200 groove/mm gratings, two $f = 10$ cm cylindrical lenses, and a transmissive π-step phase plate. The fused silica phase plate has a 882 nm step oriented at $\pm 40°$ to the grating dispersion direction. A 100 μm thick BBO crystal is located 20 cm from the output grating. (b) TG-SSSI setup, with elements described in the main text. (c) Idealized spatiotemporal intensity $I(x, \tau) \propto |E|^2$ and phase $\Delta\Phi(x, \tau)$ of (i) E_S ($l = +1$) and (ii) $E_S^{2\omega}$ ($l = +2$). (d) Spatiotemporal intensity and phase of (i) E_S ($l = +1$) and (ii) $E_S^{2\omega}$ ($l = +2$) from simulation (see Supplement 1) of our pulse shaper, followed by SHG in the nonlinear BBO crystal with $\mathrm{GVM_{BBO}} = 0$ and $\mathrm{GDD_{BBO}} = 0$. Here the diamond-like donut shape of $I_S(x, \tau)$ and $I_S^{2\omega}(x, \tau)$ stems from the contribution of higher-order Hermite–Gaussian modes generated from the π-step phase plate and superimposed on the STOV.

In order to observe the spatiotemporal phase and amplitude of the fundamental and SHG STOVs, we used transient grating single-shot supercontinuum spectral interferometry (TG-SSSI), a technique we developed for pulses containing spatiotemporal phase singularities [2,23]. TG-SSSI enables single-shot measurement of the phase $\Delta\Phi(x, \tau)$ and intensity $I(x, \tau)$ profiles of ultrashort pulses, where x is a space dimension orthogonal to pulse propagation [as shown in Fig. 1(a)] and τ is local time in the pulse frame. As shown in the TG-SSSI setup depicted in Fig. 1(b), either E_S or its second harmonic $E_S^{2\omega}$ is imaged by a low dispersion MgF_2 lens (L1) into the "witness plate", where it interferes with a spatial reference pulse ε_i to form a transient volume grating. Spectral interferometry using probe and reference supercontinuum pulses E_{pr} and E_{ref} is performed on the transient grating, enabling extraction of $\Delta\Phi(x, \tau)$ and $|E_S(x, \tau)|^2 \propto I(x, \tau)$ (or $\Delta\Phi^{2\omega}(x, \tau)$ and $|E_S^{2\omega}(x, \tau)|^2$) [2,23]. Our TG-SSSI setup can measure pulses as short as ~11 fs at the fundamental (~27 fs at the second harmonic). For adequate signal-to-noise ratio, the lowest pulse energy measured was 3 μJ, corresponding to peak intensity ~150 GW/cm^2.

A STOV-carrying pulse of center wavenumber k_0 at position $|z| \ll z_R$ along the propagation axis (strongly satisfied in these experiments) can be written as [2]

$$E_S(\mathbf{r}_\perp, z, \tau) = a\left(\frac{\tau}{\tau_s} \pm i\,\mathrm{sgn}(l)\frac{x}{x_s}\right)^{|l|} e^{ik_0 z} E_0(\mathbf{r}_\perp, z, \tau)$$

$$= A(x, \tau) e^{il\Phi_{s-t}} e^{ik_0 z} E_0(\mathbf{r}_\perp, z, \tau), \quad (1)$$

where z_R is the Rayleigh range, $\mathbf{r}_\perp = (x, y)$, $\tau = t - z/v_g$ is a time coordinate local to the pulse, v_g is the group velocity, τ_s and x_s are temporal and spatial scale widths of the STOV, $\Phi_{s-t}(x, \tau)$ is the spacetime phase circulation in $x - \tau$ space, integer is the topological charge of the STOV, $A(x, \tau) = a((\tau/\tau_s)^2 + (x/x_s)^2)^{|l|/2}$, $a = \sqrt{2}((x_0/x_s)^2 + (\tau_0/\tau_s)^2)^{-1/2}$ for $l = \pm 1$, and E_0 is the STOV-free Gaussian pulse input to the pulse shaper, where x_0 and τ_0 are the spatial and temporal widths of the pulse [2]. Here a is a normalization factor ensuring energy conservation through the pulse shaper. The propagation phase factor $e^{ik_0 z}$ contributes to extrinsic OAM, and not to the SHG process.

The well-known SHG process [24], as applied to the fundamental STOV pulse of Eq. (1), would give $E_S^{2\omega}(\mathbf{r}_\perp, z, \tau) \propto A^2(x, \tau) e^{i2l\Phi_{s-t}} E_0^2(\mathbf{r}_\perp, z, \tau)$, assuming perfect phase matching and an undepleted pump. This result is plotted in Fig. 1(c), which shows the intensity and phase of the fundamental [red colormap (i)] and second-harmonic fields [blue colormap (ii)]. The 2π phase winding of E_S is transformed into a 4π phase winding of $E_S^{2\omega}$, accompanied by a narrowing of the intensity ring by a factor $\sqrt{2}$. Because our current pulse shaper modulates only the input pulse phase and not its amplitude, the STOVs it generates are not fully symmetric as shown in the pulse shaper simulation (see Supplement 1) of Fig. 1(d-i). The diamond-shaped spacetime donut—reproduced in our measurements as seen later—results from beam contributions by higher-order Hermite–Gaussian modes generated at each frequency by the π step of the phase plate. The corresponding second-harmonic field of the shaper output is shown in Fig. 1(d-ii).

The TG-SSSI measurements of the fundamental and SHG STOVs are shown in Fig. 2, where the red colormap panels of (a) show the spatiotemporal intensity $I_S(x, \tau)$ and phase $\Delta\Phi(x, \tau)$ of the fundamental $l = +1$ STOV $E_S(x, \tau)$ at the near-field output of the 4 f pulse shaper. $I_S(x, \tau)$ has the characteristic edge-first "flying donut" profile, with the pulse propagating right to left, while $\Delta\Phi(x, \tau)$ is a single 2π winding centered at $(x, \tau) = (0, 0)$. The dip in intensity near $x = -60$ μm in Fig. 2(a) is due to scattering off the π step of the phase plate. Figure 2(b), in the blue colormap, shows the measured spatiotemporal intensity $I_S^{2\omega}(x, \tau)$ and phase $\Delta\Phi^{2\omega}(x, \tau)$ of $E_S^{2\omega}(x, \tau)$. Instead of a single $l = +2$ STOV, for which $I_S^{2\omega}(x, \tau)$ would have a single intensity null and $\Delta\Phi^{2\omega}(x, \tau)$ would have a 4π phase winding [as in Figs. 1(c) and 1(d)], we see that $I_S^{2\omega}(x, \tau)$ and $\Delta\Phi^{2\omega}(x, \tau)$ show two spatiotemporally offset vortices, embedded in the second-harmonic pulse, around whose centers are two 2π phase windings. This constitutes two $l = +1$ STOVs, and thus energy conservation dictates that the $E_S^{2\omega}$ pulse carries, on average, twice the OAM per photon of the fundamental E_S.

The spatiotemporal splitting of the STOV in $E_S^{2\omega}$ is due to (1) group velocity mismatch (GVM) ($= 1/v_g^{(2\omega)} - 1/v_g^{(\omega)}$) between the E_S^{ω} and $E_S^{2\omega}$ pulses in the BBO crystal [25] and (2) group delay

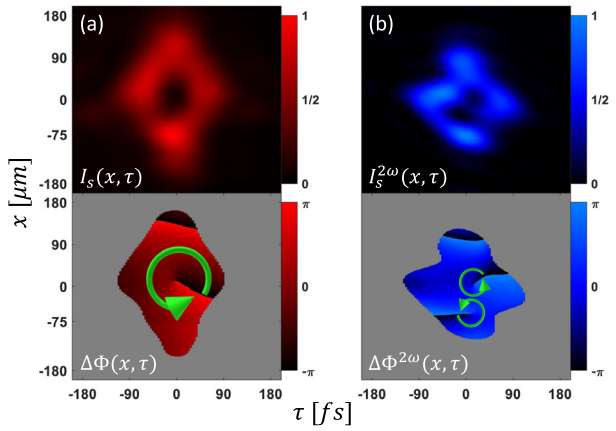

Fig. 2. TG-SSSI measurements of fundamental and SHG STOVs. (a) Top: Intensity profile $I_S(x,\tau)$ of fundamental $l=+1$ STOV; bottom: spatiotemporal phase $\Delta\Phi(x,\tau)$ showing one 2π winding. (b) Top: SHG output pulse $I_S^{2\omega}(x,\tau)$ showing two donut holes embedded in pulse; bottom: spatiotemporal phase profile $\Delta\Phi^{2\omega}(x,\tau)$ showing two 2π windings. Phase traces are blanked in regions of negligible intensity, where phase extraction fails. These images represent 500 shot averages: the extracted phase shift from each spectral interferogram is extracted, then the fringes of each frame (shot) are aligned and averaged, and then the phase map is extracted [23].

dispersion (GDD) in both the BBO and lens L1. This is demonstrated by spectral domain [$\tau\rightarrow\omega$ and $\mathbf{r}_\perp\rightarrow\mathbf{k}_\perp=(k_x,k_y)$] simulations using the carrier resolved unidirectional pulse propagation equation (UPPE) algorithm [26] of the 3D system of propagation equations

$$\partial\tilde{\mathbf{E}}/\partial z = iK_z(\omega,\mathbf{k}_\perp)\tilde{\mathbf{E}} + i2\pi K_z^{-1}(\omega,\mathbf{k}_\perp)(\omega^2/c^2)\tilde{\mathbf{P}} \quad (2)$$

for the fields $\tilde{\mathbf{E}}=\hat{\mathbf{y}}E_S$ or $\hat{\mathbf{E}}=\hat{\mathbf{x}}E_S^{2\omega}$. Here $K_z(\omega,\mathbf{k}_\perp)=\sqrt{k^2(\omega)-|\mathbf{k}_\perp|^2}$ is the linear propagator in the spectral domain, $k(\omega)=\omega n(\omega)/c$ is the wavenumber (with dispersion in BBO and MgF_2 lens L1 provided by Refs. [25] and [27]), and $\tilde{\mathbf{P}}$ is the nonlinear polarization for the BBO portion of the propagation, where the orthogonally polarized E_S^{ω} and $E_S^{2\omega}$ fields are computed in the spatiotemporal domain and coupled through

$$P_y = \chi^{(2)}_{yxy}(-\omega;2\omega,-\omega)E_xE_y^*e^{-i(k_y+k_y-k_x)z}$$

$$P_x = (1/2)\chi^{(2)}_{xyy}(-2\omega;\omega,\omega)E_y^2e^{i(k_y+k_y-k_x)z},$$

where $\chi^{(2)}$ is the second-order susceptibility tensor for BBO [28].

Owing to symmetry along y, we used $\partial\tilde{\mathbf{E}}/\partial y=0$, which also reduces the computational load. The simulation (see Supplement 1) generates E_S in the pulse shaper, propagates it through the BBO while generating $E_S^{2\omega}$, and then propagates the fields through MgF_2 lens L1 to the witness plate. The initial conditions at the entrance to the pulse shaper are $\hat{\mathbf{x}}\,E_x=0$, and $\hat{\mathbf{y}}E_0$ is a plane wave with wavevector $(0,0,k_0)$, where $|E_0|^2$ is a Gaussian corresponding to the experiment's 3.2 mm $1/e^2$ beam radius, 50 fs pulse width, and 350 μJ energy.

Our simulations generating $E_S^{2\omega}(\mathbf{r}_\perp,z,\tau)$ show that for the case of zero dispersion ($GVM_{BBO}=0$, $GDD_{BBO}=0$, and $GDD_{L1}=0$), the $l=+2$ STOV does not break up for BBO crystal thickness less than ~100 μm. This is seen in Fig. 3(a) for two BBO thicknesses, 20 μm and 100 μm. The $\Delta\Phi^{2\omega}(x,\tau)$ plots are zoomed in near the phase singularity, while the insets show the full intensity profile.

Figure 3(b) shows a simulation for the case of $GVM_{BBO}=0.19\ fs^2/\mu m$ and $GDD_{BBO}=0$. We conclude that nonzero GVM_{BBO} is sufficient to break the $l=+2$ STOV into two $l=+1$ STOVs in as little as 20 μm of propagation in BBO. Including $GDD_{BBO}=20.9\ fs^2$ in the simulation [Fig. 3(c)] slows the separation of the two windings relative to the case in Fig. 3(b). We note that for $I_S^{2\omega}(x,\tau)$ [insets of (a), (b), and (c)], the two field nulls are resolvable only into one central null.

A simulation corresponding directly to Fig. 2's experimental parameters is shown in Fig. 3(d), where $GDD_{L1}=350\ fs^2$ and $GDD_{air}=250\ fs^2$ are included. Here, the already separated $l=+1$ STOVs are driven farther apart by the additional GDD_{L1},

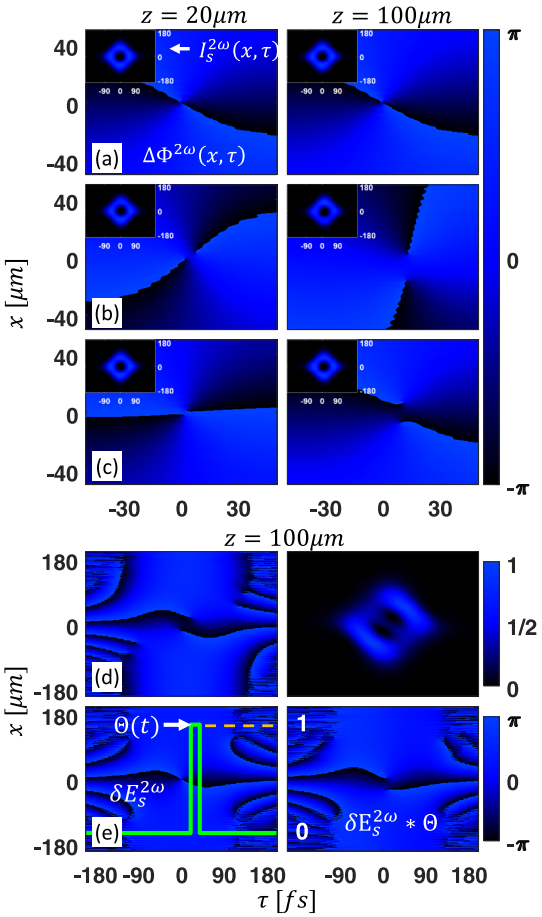

Fig. 3. Simulation (see Supplement 1) of the SHG of $l=+1$ STOV pulse E_S. Plotted are $I_S^{2\omega}(x,\tau)\propto|E_S^{2\omega}|^2$ and $\Delta\Phi^{2\omega}(x,\tau)$, the intensity and phase of the simulated SHG pulse. The simulation generates E_S in the pulse shaper, propagates it through the BBO while generating $E_S^{2\omega}$, and then propagates the fields through MgF_2 lens L1 to the witness plate. The phase images are zoomed in at the null to show the decomposition of the high-order STOV. (a) $GVM_{BBO}=0$, $GDD_{BBO}=0$, $GDD_{L1}=0$. The $l=2$ STOV does not break up regardless of the BBO thickness, here for 20 μm (left) and 100 μm (right). Insets: $I_S^{2\omega}(x,\tau)$, with horizontal τ (fs) and vertical x (μm) scales. (b) $GVM_{BBO}=0.19\ fs^2/\mu m$, $GDD_{BBO}=0$, and $GDD_{L1}=0$. Here, the $l=2$ STOV breaks up into two $l=1$ STOVs in as little as 20 μm. (c) $GVM_{BBO}=0.19\ fs^2/\mu m$, $GDD_{BBO}=20.9\ fs^2$, and $GDD_{L1}=0$. (d) Simulation corresponding to experimental parameters of Fig. 2: $GVM_{BBO}=0.19\ fs^2/\mu m$, $GDD_{BBO}=20.9\ fs^2$, $GDD_{air}=250\ fs^2$, and $GDD_{L1}=350\ fs^2$. (e) Convolution model of the effect of GVM in BBO, showing decomposition of $l=+2$ STOV into two $l=+1$ STOVs.

leading to two spatiotemporally offset nulls in $I_S^{2\omega}(x,\tau)$. Because of linear propagation in L1, $\mathrm{GDD_{L1}}$ has a different effect than the interplay of $\mathrm{GVM_{BBO}}$ and $\mathrm{GDD_{BBO}}$ on vortex separation during nonlinear propagation [Fig. 3(c)]. Comparing the results in Figs. 2(b) and 3(c), the simulation matches the experiment quite well.

The effect of GVM in the BBO on the decomposition of an $l=+2$ STOV can be explained as follows: As E_S propagates in the BBO, each portion of its envelope at local time τ nonlinearly generates a contribution $\delta E_S^{2\omega}$ that slips back in time. The SHG crystal output can then be constructed as the convolution $E_S^{2\omega}(x,\tau)=\int_{-\infty}^{\tau}\delta E_S^{2\omega}(x,\tau-t)\Theta(t)\mathrm{d}t$, the sum of a sequence of time-shifted $l=+2$ STOV contributions $\delta E_S^{2\omega}(x,\tau-t)$ that models the increasing slip of the peak of $E_S^{2\omega}$ with respect to the peak of E_S. Here $\Theta(t)=1$ for $0\le t\le\Delta\tau$, and $\Theta(t)=0$ elsewhere, where the maximum time slip is $\Delta\tau=(1/v_g^{(2\omega)}-1/v_g^{(\omega)})L\approx 19$ fs for the SHG crystal length $L=100$ μm. The integral yields two spatially offset $l=+1$ STOVs as depicted in Fig. 3(d). This is essentially the STOV equivalent to the splitting observed due to spatial walk-off of LG beams in nonlinear crystals [29]. The addition of nonzero $\mathrm{GDD_{L1}}$ leads to the diagonal (spatiotemporal) offset of Fig. 3(c). Recognizing from Fig. 3 that the two spatiotemporally offset $l=+1$ STOVs represents a superposition of time-shifted $l=+2$ STOV pulses, we find that OAM conservation in SHG also applies to STOVs.

In summary, we have experimentally and theoretically demonstrated the conservation of STOV-based OAM in SHG. GVM between the fundamental and second-harmonic STOVs is the primary cause for $l=+2$ STOVs to quickly separate into two $l=+1$ STOVs after only a short propagation distance in the SHG crystal. The spacetime separation of STOVs during SHG could be mitigated via group velocity matching by using noncollinear SHG geometry.

The question of whether photons in an ultrashort STOV pulse individually carry transverse OAM is difficult to answer experimentally in linear optics; this question is more easily answered with the help of nonlinear optics. The conservation of photon number implied by the Manley–Rowe relation for SHG, $2d/dz(I^{(\omega)}/\hbar\omega)=d/dz(I^{(2\omega)}/\hbar\omega)$ [24], implies that, *on average*, photons at the second harmonic carry twice the OAM of photons at the fundamental. However, because SHG is fundamentally a quantum mechanical process involving light–matter interactions of the quantized electromagnetic field, and because all photons in the STOV pulse from our pulse shaper carry the same bandwidth, polarization, and spatiotemporal phase, we conclude that energy and angular momentum conservation in the SHG process holds at the individual photon level—and that photons in STOV-carrying pulses have OAM orthogonal to their direction of propagation. The uncertainty relations $\Delta k_x\Delta x\ge 1/2$ and $\Delta k_\xi\Delta\xi\ge 1/2$ ensure that a photon with STOV OAM could be found anywhere in the transverse and longitudinal extent of the pulse, and it could have any frequency consistent with the bandwidth.

Funding. National Science Foundation (PHY2010511); Office of Naval Research (N00014-17-1-2705, N00014-20-1-2233); Air Force Office of Scientific Research (FA9550-16-1-0121, FA9550-16-1-0284).

Acknowledgment. The authors thank I. Larkin and R. Schwartz for discussions and technical assistance.

Disclosures. The authors declare no conflicts of interest.

Data Availability. Data underlying the results presented in this paper are not publicly available at this time but may be obtained from the authors upon reasonable request.

Supplemental document. See Supplement 1 for supporting content.

REFERENCES

1. N. Jhajj, I. Larkin, E. W. Rosenthal, S. Zahedpour, J. K. Wahlstrand, and H. M. Milchberg, Phys. Rev. X. **6**, 031037 (2016).
2. S. W. Hancock, S. Zahedpour, A. Goffin, and H. M. Milchberg, Optica **6**, 1547 (2019).
3. K. Y. Bliokh and F. Nori, Phys. Rev. A **86**, 033824 (2012).
4. L. Allen, M. W. Beijersbergen, R. J. C. Spreuw, and J. P. Woerdman, Phys. Rev. A **45**, 8185 (1992).
5. M. Musigmann and J. Jahns, J. Opt. Soc. Am. B **33**, 574 (2016).
6. N. Papasimakis, T. Raybould, V. A. Fedotov, D. P. Tsai, I. Youngs, and N. I. Zheludev, Phys. Rev. B. **97**, 201409 (2018).
7. A. Vincotte and L. Bergé, Phys. Rev. Lett. **95**, 193901 (2005).
8. N. Jhajj, "Hydrodynamics and electrodynamic implications of optical femtosecond filamentation," Ph.D. dissertation (University of Maryland, 2017).
9. S. Zahedpour, S. W. Hancock, and H. M. Milchberg, in *Frontiers in Optics + Laser Science APS/DLS, OSA Technical Digest* (Optical Society of America 2019), paper FW5F.5.
10. A. Chong, C. Wan, J. Chen, and Q. Zhan, Nat. Photonics **14**, 350 (2020).
11. J. Courtial, K. Dholakia, L. Allen, and M. J. Padgett, Phys. Rev. A **56**, 4193 (1997).
12. X. Fang, Z. Kuang, P. Chen, H. Yang, Q. Li, W. Hu, Y. Lu, Y. Zhang, and M. Xiao, Opt. Lett. **42**, 4387 (2017).
13. V. N. Belyi, N. A. Khilo, N. S. Kazak, A. A. Ryzhevich, and A. Forbes, Opt. Eng. **50**, 059001 (2011).
14. K. Dai, W. Li, K. S. Morgan, Y. Li, J. K. Miller, R. J. Watkins, and E. G. Johnson, Opt. Express. **28**, 2536 (2020).
15. R. Ni, Y. F. Niu, L. Du, X. P. Hu, Y. Zhang, and S. N. Zhu, Appl. Phys. Lett. **109**, 151103 (2016).
16. Y. Li, Z.-Y. Zhou, D.-S. Ding, and B.-S. Shi, J. Opt. Soc. Am. B **32**, 407 (2015).
17. G. Gariepy, J. Leach, K. T. Kim, T. J. Hammond, E. Frumker, R. W. Boyd, and P. B. Corkum, Phys. Rev. Lett. **113**, 153901 (2014).
18. S. Li, B. Shen, X. Zhang, Z. Bu, and W. Gong, Opt. Express **26**, 23460 (2018).
19. F. Kong, C. Zhang, F. Bouchard, Z. Li, G. G. Brown, D. H. Ko, T. J. Hammond, L. Arissian, R. W. Boyd, E. Karimi, and P. B. Corkum, Nat. Commun. **8**, 14970 (2017).
20. D. Gauthier, P. Rebernik Ribič, G. Adhikary, A. Camper, C. Chappuis, R. Cucini, L. F. DiMauro, G. Dovillaire, F. Frassetto, R. Géneaux, P. Poletto, B. Ressel, C. Spezzani, M. Stupar, T. Ruchon, and G. De Ninno, Nat. Commun. **8**, 14971 (2017).
21. S. W. Hancock, S. Zahedpour, and H. M. Milchberg, in *Frontiers in Optics + Laser Science APS/DLS, OSA Technical Digest* (Optical Society of America 2020), paper FM7C.6.
22. S. W. Hancock, S. Zahedpour, and H. M. Milchberg, in *High-brightness Sources and Light-driven Interactions Congress, OSA Technical Digest* (Optical Society of America 2020), paper JM3A.21.
23. S. W. Hancock, S. Zahedpour, and H. M. Milchberg, Opt. Lett. **46**, 1013 (2021).
24. R. W. Boyd, in *Nonlinear Optics* (Academic, 2008), pp. 69–133.
25. D. Eimerl, L. Davis, and S. Velsko, J. Appl. Phys. **62**, 1968 (1987).
26. A. Couairon, E. Brambilla, T. Corti, D. Majus, O. de J. Ramírez-Góngora, and M. Kolesik, Eur. Phys. J. Spec. Top. **199**, 5 (2011).
27. M. N. Polyanskiy, "Refractive index database," 2020, https://refractiveindex.info.
28. R. C. Eckardt, H. Masuda, Y. X. Fan, and R. L. Byer, IEEE J. Quantum Electron. **26**, 922 (1990).
29. Y. Toda, S. Honda, and R. Morita, Opt. Express **18**, 17796 (2010).